nature communications

Article

https://doi.org/10.1038/s41467-024-51387-6

Lightweight single-phase Al-based complex concentrated alloy with high specific strength

Received: 24 January 2024

Accepted: 5 August 2024

Mingliang Han[1,2,3], Yuan Wu[1,3] ✉, Xiaobin Zong[1], Yaozu Shen[1] ✉, Fei Zhang[2,4], Hongbo Lou[2,5], Xiao Dong[6], Zhidan Zeng[2], Xiangyang Peng[7], Shuo Hou[7], Guangyao Lu[7], Lianghua Xiong[8], Bingmin Yan[2], Huiyang Gou[2], Yanping Yang[2], Xueyan Du[2], Xiaoyuan Yuan[1], Yingjie Zhang[1], Meiyuan Jiao[1], Xiongjun Liu[1], Suihe Jiang[1], Hui Wang[1], Andrey A. Rempel[9], Xiaobin Zhang[1] ✉, Qiaoshi Zeng[2,5] ✉ & Z. P. Lu[1]

Developing light yet strong aluminum (Al)-based alloys has been attracting unremitting efforts due to the soaring demand for energy-efficient structural materials. However, this endeavor is impeded by the limited solubility of other lighter components in Al. Here, we propose to surmount this challenge by converting multiple brittle phases into a ductile solid solution in Al-based complex concentrated alloys (CCA) by applying high pressure and temperature. We successfully develop a face-centered cubic single-phase Al-based CCA, $Al_{55}Mg_{35}Li_5Zn_5$, with a low density of 2.40 g/cm^3 and a high specific yield strength of 344×10^3 N·m/kg (typically ~ 200×10^3 N·m/kg in conventional Al-based alloys). Our analysis reveals that formation of the single-phase CCA can be attributed to the decreased difference in atomic size and electronegativity between the solute elements and Al under high pressure, as well as the synergistic high entropy effect caused by high temperature and high pressure. The increase in strength originates mainly from high solid solution and nanoscale chemical fluctuations. Our findings could offer a viable route to explore lightweight single-phase CCAs in a vast composition-temperature-pressure space with enhanced mechanical properties.

The combination of lightweight and high strength, namely high specific strength, can effectively reduce the weight of materials needed to meet the mechanical requirements in various structural applications. Due to the increasing demand to reduce energy consumption and carbon emissions, the pursuit of lightweight and high-strength metallic materials has attracted considerable attention from a wide range of industries, especially in the field of transportation. Al-based alloys are featured by their low density (one-third of that of steel, copper, or

---

[1]State Key Laboratory for Advanced Metals and Materials, University of Science and Technology Beijing, Beijing 100083, China. [2]Center for High Pressure Science and Technology Advanced Research, Shanghai 201203, China. [3]Institute of Materials Intelligent Technology, Liaoning Academy of Materials, Shenyang 110004, China. [4]Institute of High Energy Physics, Chinese Academy of Sciences, Beijing 100049, China. [5]Shanghai Key Laboratory of Material Frontiers Research in Extreme Environments (MFree), Institute for Shanghai Advanced Research in Physical Sciences (SHARPS), Shanghai 201203, China. [6]Key Laboratory of Weak-Light Nonlinear Photonics and School of Physics, Nankai University, Tianjin 300071, China. [7]Equipment Research Center, China Nuclear Power Technology Research Institute Co., Ltd., Shenzhen 518000, China. [8]Shanghai Key Laboratory of Advanced High-temperature Materials and Precision Forming, School of Materials Science and Engineering, Shanghai Jiao Tong University, Shanghai 200240, China. [9]Institute of Metallurgy of the Ural Branch of the Russian Academy of Sciences, 620016 Ekaterinburg, Russia. ✉e-mail: wuyuan@ustb.edu.cn; shenyaozu@ustb.edu.cn; zhangxb@ustb.edu.cn; zengqs@hpstar.ac.cn

brass), weak magnetism, and high specific strength, making them the most popular lightweight engineering materials capable of widespread application[1].

However, developing lighter Al-based alloys needs to introduce additional amounts of lighter elements. Nevertheless, exceeding the solubility limit of these elements in Al could lead to the alloy being mostly composed of intermetallic compounds (IMCs), lacking a ductile FCC matrix, thereby resulting in deterioration in mechanical performance. This limitation impedes the advancement of light Al-based alloys.

In addition, achieving high specific strength in Al-based alloys is challenging as strength typically decreases with decreasing density[2]. In other words, alloy design and preparation approaches are needed to overcome these obstacles in developing lightweight Al-based alloys with high specific strength.

Recently, introducing high configurational entropy based on the concept of CCAs has proven to be an effective way to stabilize solid solution phases against forming IMCs far beyond their traditional solubility limits. Although numerous Al-containing CCAs were reported[3–7], their microstructure still exhibits a mixture of excessive IMCs[8–11], which may not provide sufficient slip systems for plastic deformation, or promote easy crack propagation along grain boundaries, resulting in deterioration of mechanical properties and performance[12].

The lack of single-phase solid solution Al-based CCAs is attributed to the significant differences in atomic radius and electronegativity between Al and other light elements[13], resulting in high mixing enthalpy (H) and low excess configurational entropy (S_E). In this case, the formation of chemically ordered IMCs is energetically favored.

Elevating temperatures usually enhance the solubility of one element in another due to the enhanced entropy effect. However, in the case of Al-based alloys, IMCs still easily form during solidification by quenching high-temperature melts, indicating that the entropy effect generated solely by increasing temperature is still insufficient. In addition to composition and temperature, pressure has also been reported as an effective tool for altering phase stability[14,15], and even promoting phase transitions from binary intermetallic compounds to random solid solutions[14]. Therefore, by combining high temperature with high pressure, many novel materials otherwise inaccessible by traditional processing methods have been obtained, such as magnetic materials, superconductive materials[16], and ultrahard materials[17–19]. Rich phase transitions have also been reported in many binary lightweight alloys under high-temperature and high-pressure conditions[20–22], providing a promising approach for developing lightweight Al-based alloys.

In this work, we developed a low-density (2.4 g/cm^3) and high specific yield strength (344×10^3 N·m/kg) $Al_{55}Mg_{35}Li_5Zn_5$ CCA with a single-phase face-centered cubic (SP-FCC) structure by applying high pressure and high temperature (HPHT) to promote the transition from IMCs to solid solutions. The formation of the SP-FCC lattice is attributed to the decreased differences in atomic size and electronegativity between the solute elements and Al under high pressure, as well as the synergistic high entropy effect caused by high temperature and high pressure. The distinct solid solution strengthening comes from the incorporation of multiple elements in one single FCC lattice, as well as the significant pinning effect of dislocations from nanoscale chemical fluctuations, which leads to the enhanced strength of the low-density CCA.

Results

Structure characterization

Aiming to lower the density of Al-based alloys and maintain their strength, we have to select an appropriate alloy system with a proper composition. First, to develop Al-based alloys with lower density without sacrifice of strength, two other types of elements can be incorporated into the Al alloy. One is the light elements with a high strength-to-weight ratio, such as Mg or Li, to increase the resultant strength and stiffness without adding weight. The other type is the element that can provide benefits like corrosion resistance and thermal stability such as Zn. Second, the atomic ratio of these elements can be optimized by considering local atomic strains, namely the λ value, as elaborated in Supplementary Note 1 and Supplementary Figs. 1 and 2. Target samples (~ 2 mm in diameter and ~ 3 mm in height) with a nominal composition of $Al_{55}Mg_{35}Li_5Zn_5$ were synthesized using a multi-anvil large volume press (LVP). The schematic drawing of the high-pressure cell assembly of LVP is shown in Supplementary Fig. 3.

Synchrotron X-ray diffraction (XRD) experiments were performed on the as-cast samples and the HPHT-synthesized samples to characterize their phase constituents. The HPHT condition was determined based on dependence of λ on temperature and pressure, as well as experimental verifications. First, the λ value decreases with the increase of pressure applied. When the pressure is increased to a certain value at which the λ value decreases to below 0.11, then a solid solution is likely formed, as shown in Supplementary Fig. 2. Second, high temperature amplifies the contribution of entropy, which can decrease the total free energy and thermodynamically stabilize solid solution against IMCs. Thus, elevating temperature can promote long-range atomic diffusion required to form a single phase from the initial mixture containing multiple IMCs. Therefore, as the pressure increases, the critical temperature for the formation of single-phase decreases. As can be seen in Supplementary Fig. 4, with the increase of the applied pressure, the critical temperature for forming a single-phase FCC structure in $Al_{55}Mg_{35}Li_5Zn_5$ decreases from 1410 to 1280 K. Based on the λ design principle, we explored a series of alloys under various pressures ranging from 8 GPa to 30 GPa and temperatures up to 2000 K to determine the optimal HPHT conditions (see Supplementary Note 2 and Supplementary Fig. 5 for details). Considering both experimental feasibility and cost-effectiveness, we have opted for a moderate HPHT condition, namely 15 GPa and 1500 K, to synthesize bulk SP-FCC samples.

Figure 1a shows synchrotron XRD patterns of the as-cast sample and the HPHT-synthesized sample recovered from 15 GPa and 1500 K. Clearly, the as-cast sample contains multiple IMCs, including Al_3Mg_2, $LiMgAl_2$, and $Mg_{32}(AlZn)_{49}$ phases. In contrast, for the HPHT-synthesized sample, only crystalline peaks corresponding to an FCC lattice (i.e., space group: Fm $\bar{3}$ m, $a = 4.203$ Å) can be seen, indicating that this sample possesses a single-phase structure. The high-resolution transmission electron microscopy (HRTEM) image and the corresponding selected area electron diffraction (SAED) pattern also confirm the SP-FCC structure, as shown in Fig. 1b, c, respectively. In addition, a fairly uniform distribution of numerous dislocations was also observed in the HPHT-synthesized sample in the bright-field TEM image (Fig. 1d). Electron backscatter diffraction (EBSD) image reveals an equiaxed grain morphology of the HPHT-synthesized sample (Fig. 1e). Energy dispersive spectroscopy (EDS) elemental mapping of the as-cast sample shows that Al, Mg, and Zn are enriched in different phase regions, whilst the HPHT-synthesized sample exhibits a spatially uniform distribution of all constituents (Supplementary Fig. 6). Therefore, a single-phase $Al_{55}Mg_{35}Li_5Zn_5$ CCA is obtained via the HPHT treatment.

More detailed chemical distribution with atomic scale resolution of the HPHT-synthesized sample was further examined by three-dimensional atom probe tomography (3D-APT). Iso-concentration maps of Li (5.8 at.%), Zn (8 at.%) and their overlap were displayed to depict local chemical fluctuations (Fig. 1f), in which morphology of nanoscale chemical fluctuations enriched with Li and Zn is revealed. The composition analysis along a line crossing the interface between the matrix and nanoscale clusters is presented in Fig. 1g. As can be seen, all components in the FCC solid solution matrix distributed homogenously. Within clusters (the right side of Fig. 1g),

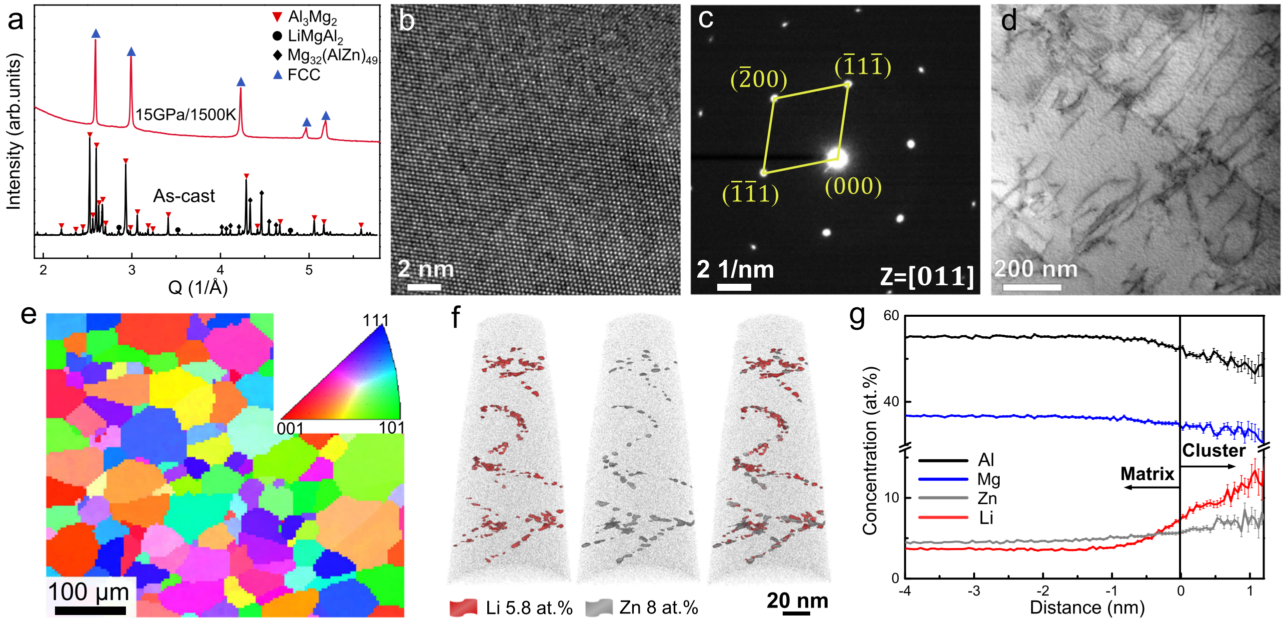

Fig. 1 | Characterization of the as-cast and HPHT-synthesized $Al_{55}Mg_{35}Li_5Zn_5$ samples. a Synchrotron XRD patterns of the as-cast sample (black) and the sample synthesized at 15 GPa and 1500 K by LVP (red). **b**, **c** HRTEM and SAED images of the HPHT-synthesized sample, revealing an SP-FCC structure. The SAED pattern is obtained along the [011] direction. **d** Bright-field TEM image, showing a fairly uniform distribution of numerous dislocations in the HPHT-synthesized sample. **e** EBSD image of the HPHT-synthesized sample, showing the grains with different orientations. The inset shows the orientations corresponding to different colors. **f** APT reconstruction of the HPHT-synthesized sample. Maps of 5.8 at.% Li, 8 at.% Zn iso-concentration and their overlap are displayed to depict local chemical fluctuations. **g** Composition analysis along a line crossing the interface between the matrix and nanoscale clusters. The error bars are standard deviations of the mean.

concentrations of Li and Zn reach ~ 12 and ~ 8.5 at.%, respectively, whilst Al and Mg are correspondingly depleted. The formation of these nanoscale chemical fluctuations seems to be closely related to the synergistic effects of high pressure and high temperature, as well as the high entropy effect. Initially, plastic deformation induced by phase transitions or non-hydrostatic pressure components under high pressure can introduce numerous dislocations, as reported in severe plastic deformation studies[23]. Actually, dislocations in crystalline solid solutions are disturbed regions capable of inducing solute segregation when diffusion is enabled, potentially reducing the system energy[24,25]. Subsequent heating processes then enhanced the driving force for the diffusion of Li and Zn solutes (Li and Zn have larger atomic radii and electronegativity differences with Al) towards these dislocations, promoting the formation of nanoscale chemical fluctuations. Also, it is recognized that nanoscale chemical fluctuations are a common structure feature for CCAs because of the large chemical complexity resulting from the high configuration entropy[26].

Mechanical properties

Figure 2a shows room-temperature compressive stress-strain curves of the as-cast sample (black) and the HPHT-synthesized $Al_{55}Mg_{35}Li_5Zn_5$ CCA (red). The as-cast alloy failed at ~ 280 MPa without obvious yielding and fragmented into many pieces (Supplementary Fig. 7), showing a brittle fracture behavior. In contrast, the yield strength was substantially enhanced by almost three times to 825 MPa for the SP-FCC CCA, accompanied by an increased total compressive strain from ~ 1% to ~ 4 %. The fracture mode changed from the shattering failure of the as-cast sample containing multiphase IMCs to the fracture along the ~ 45° direction of the SP-FCC CCA (see the inset of Fig. 2a).

Figure 2b shows the comparison of the specific yield strength and density between the SP-FCC $Al_{55}Mg_{35}Li_5Zn_5$ CCA and previously reported Al-based CCAs, Ti-based CCAs, AlTiNb-based CCAs, and other lightweight CCAs (See Supplementary Table 1 for detailed composition information). The developed $Al_{55}Mg_{35}Li_5Zn_5$ CCA, which is located at the top-left regime, has the highest specific yield strength (344×10^3 N·m/kg) and nearly the lowest density (2.4 g/cm^3), outperforming most of the reported CCAs. More information on the density comparison with other Al-based alloys is shown in Supplementary Fig. 8. It can be seen that the SP-FCC $Al_{55}Mg_{35}Li_5Zn_5$ CCA possesses an low density of 2.4 g/cm^3, lower than that of most Al alloys (~ 2.8 g/cm^3), including Al-Li alloys (~ 2.5–2.9 g/cm^3) and 5xxx series Al alloys (~ 2.65 g/cm^3).

Deformation behavior analysis

Figure 3a, b show fractured surfaces of the as-cast and HPHT-synthesized specimens, respectively. The fracture surface of the as-cast alloy is smooth with very limited deformation features, whereas the HPHT-synthesized CCA exhibits transgranular fracture behavior with clear cleavage steps and river patterns. To further investigate the deformation mechanism of the HPHT-synthesized SP-FCC $Al_{55}Mg_{35}Li_5Zn_5$ alloy, we conducted TEM characterization of the fractured samples. As can be seen from the bright-field TEM image of the fractured SP-FCC sample (Fig. 3c), numerous dislocations were observed throughout the matrix, and well-developed planar slip bands (indicated by yellow arrows) appeared, indicating that the plastic deformation is dominated by planar slip. The corresponding SAED of the fractured sample confirms neither phase transformation nor twinning after deformation (Fig. 3d). As shown in Supplementary Fig. 7, the as-cast sample consisting of multiple IMCs fractured in a brittle mode with limited dislocation operation, which can be attributed to insufficient slip systems and weak grain boundaries between IMCs and matrix[12]. For the SP-FCC sample, weak grain boundaries were eliminated due to the suppression of IMCs, and planar slip dominated the deformation process with massive dislocations.

Discussion

To reveal the phase transition mechanism from multiple IMCs to the SP-FCC solid solution, in situ high-pressure (laser heating) XRD measurements were conducted using a diamond anvil cell (DAC). Firstly,

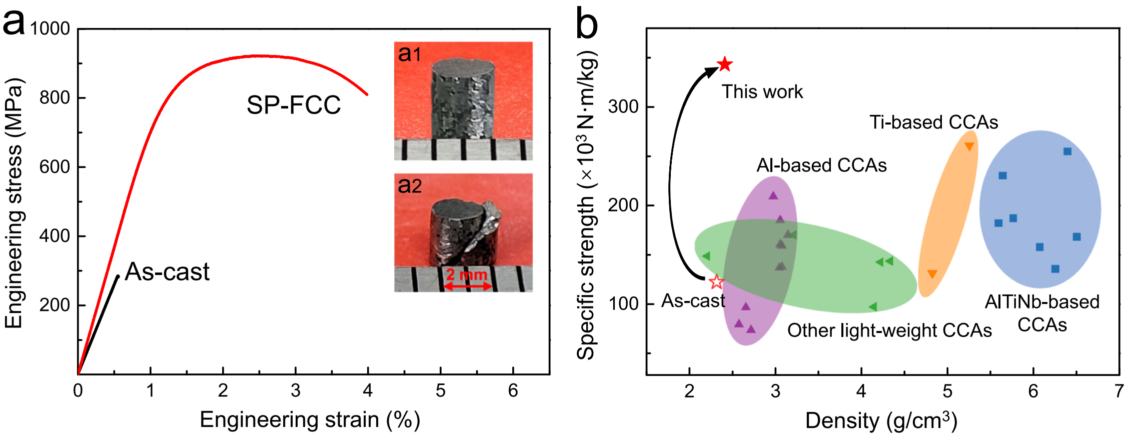

Fig. 2 | Mechanical properties. a Stress-strain curves of the as-cast and SP-FCC $Al_{55}Mg_{35}Li_5Zn_5$ CCAs at room temperature under compression. The insets **a1** and **a2** are the optical images of the SP-FCC sample before and after compression, respectively. **b** Specific fracture strength and density of the SP-FCC $Al_{55}Mg_{35}Li_5Zn_5$ CCA, in comparison with those of various lightweight CCAs. The data of other alloys are taken from literature[8,62–69]. Different colored shadows and symbols represent the performance of different CCAs.

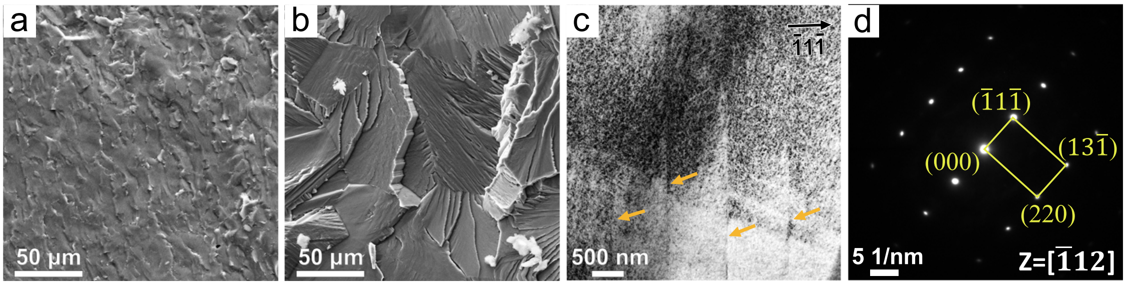

Fig. 3 | Deformation behavior of the SP-FCC $Al_{55}Mg_{35}Li_5Zn_5$ CCA. a, b Fracture surfaces of the as-cast and SP-FCC $Al_{55}Mg_{35}Li_5Zn_5$ CCAs, respectively. **c** Representative bright-field TEM image of dislocation morphologies in a fractured SP-FCC sample, imaged under (−112) type diffraction conditions. **d** The corresponding SAED pattern along the [−112] direction of the fractured SP-FCC sample.

in situ high-pressure XRD was performed on the starting $Al_{55}Mg_{35}Li_5Zn_5$ alloy at room temperature to verify the pressure effect. As shown in Fig. 4a, the starting sample initially shows multiple IMCs including Al_3Mg_2, $LiMgAl_2$, $Mg_{32}(AlZn)_{49}$ and other IMCs. With the increase of compression pressure up to 22 GPa, no phase transition occurred at room temperature, indicating that applying pressure alone could not obtain the SP-FCC solid solution phase. Note that NaCl served as the pressure-transmitting medium and thermal insulator, as indicated in Fig. 4.

Therefore, in situ HPHT laser heating XRD measurements on the as-cast $Al_{55}Mg_{35}Li_5Zn_5$ alloy at 10 GPa were further performed to uncover the effects of both pressure and temperature (Fig. 4b). Below 950 K, all diffraction peaks of the IMCs remained almost unchanged, indicating that those IMCs in the as-cast alloy are stable up to ~ 950 K at 10 GPa. With the further increase of temperature, new diffraction peaks corresponding to the FCC lattice appeared and gradually grew with increasing temperature at the expense of the IMCs peaks. Eventually, all peaks related to IMCs disappeared at ~ 1410 K.

Generally, high configuration entropy tends to stabilize random solid-solution phases at high temperatures[27]. However, whether a single solid solution phase is ultimately formed also depends on the enthalpy of mixing (the interaction between each component). The existence of multiple IMCs in the as-cast $Al_{55}Mg_{35}Li_5Zn_5$ sample at ambient pressure could be attributed to the relatively high mixing enthalpy between the constituents.

According to the empirical Hume-Rothery rules, the formation of multiple IMCs against solid solutions results from significant differences in atomic size and electronegativity. A large difference in electronegativity indicates strong chemical interactions between the components, while large atomic size mismatches often create large local atomic strain, which tends to destabilize solid solutions.

Specifically, based on the atomic scale elasticity theory, a λ parameter was proposed to estimate the local atomic strain resulted from atomic size mismatch[28]. The parameter λ can be expressed[29] as $\lambda = \sum_{i=B}^{Z} C_i \left| \left(r_i / r_a \right)^3 - 1 \right|$, where C_i is the solute concentration, r_i and r_a are the atomic radius of the solute and solvent (Al) atoms, respectively. Essentially, λ is a parameter used to measure the instability of solid solutions. A small value of λ implies a small strain in the matrix, indicating high stability of the solid solution. If λ exceeds a certain threshold, the matrix would become topologically unstable, resulting in destabilization of the solid solution. Moreover, based on statistical analysis of multiple Al-based alloys[28,29], the critical threshold for solid solution destabilization in Al-based alloys was found to be $\lambda > 0.1$. At the ambient pressure, $Al_{55}Mg_{35}Li_5Zn_5$ shows the lowest λ value (i.e., ~ 0.156), indicating a significant potential for forming SP-FCC, although it contains multiple IMCs at room temperature.

Fortunately, pressure is an effective tool for altering the atomic radius and electronegativity in alloys[14,15]. For most elements, electronegativity typically decreases with pressure, which is consistent with the general trend of pressure-induced metallization[30]. If the differences in atomic size and electronegativity between each component both decrease with increasing pressure, the Hume-Rothery rules

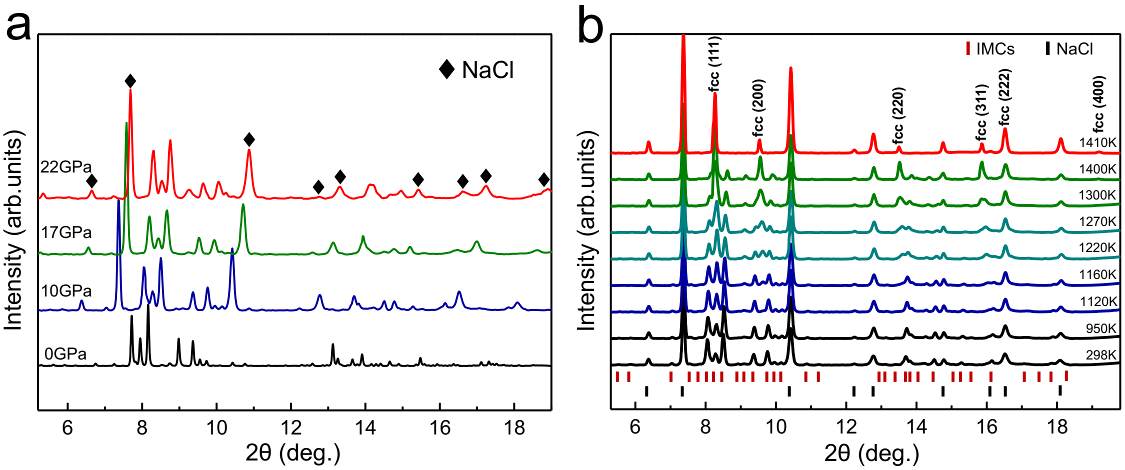

Fig. 4 | Phase evolution at high pressures. a Synchrotron XRD patterns of the as-cast $Al_{55}Mg_{35}Li_5Zn_5$ alloy during compression up to 22 GPa at room temperature. No phase transition was observed. **b** Synchrotron XRD patterns of the $Al_{55}Mg_{35}Li_5Zn_5$ alloy as a function of temperature when subjected to a compression pressure of 10 GPa. The intermetallic compounds (IMCs) in the as-cast alloy remained stable up to ~ 950 K at 10 GPa, then a phase transition started at ~ 950 K. NaCl served as the pressure-transmitting medium and thermal insulator here. The red and black tick marks in Fig. 4b represent the peaks of IMCs and NaCl.

can be satisfied and the formation of solid solutions will be favored thermodynamically by simultaneously applying pressure and temperature[14]. The equation of state of Al, Mg, Zn, and Li has been well studied and available in literature[31–35], allowing for a simple calculation of their pressure-dependent atomic radii (Fig. 5a). Our high-pressure synthesized $Al_{55}Mg_{35}Li_5Zn_5$ alloy is a solid solution with a single FCC lattice structure, and the atoms inside this specific alloy are in a “free” state. Therefore, in our opinion, it is reasonable to use the information regarding the pressure-atomic size relationship of pure metals to understand the transformation behavior of this alloy. It is obvious that the atomic radius decreases with pressure but with a quite different rate for each component, which naturally yields the changes in atomic size difference under pressure. The changes are more quantitatively reflected by the calculated parameter λ as a function of applied pressure in Fig. 5b. As seen, the λ value decreases with increasing pressure. At ~ 15 GPa, λ drops below the critical value of 0.1, indicating that the formation of a single solid solution is favorable, which is consistent with our experimental observations.

It is to note that the reduction in atomic radius difference between Mg and Al is larger than that between Zn and Al. This trend leads to an increase in the solubility of Mg in Al with the increase of pressure. With the increase of pressure, the radius value of Li sharply declines and quickly reaches the same value as Al. Therefore, from the perspective of atomic size mismatch, the solid solubility of Li in Al increases with the increase of pressure. In addition to pressure, high temperatures can also change the size difference in the four elements. Accordingly, we have analyzed the size change of four elements with temperature (see Supplementary Note 3 and Supplementary Fig. 9, Table 2), and found that the temperature effect can be neglected, as compared with the pressure effect.

In addition, the difference in electronegativity between components should also be considered. The electronegativity of the four components as a function of pressure can be obtained through the theoretical calculation method (details are included in Methods)[30] (Fig. 5c). In the range of 10-20 GPa, the electronegativity of Mg and Al intersect with each other, which is beneficial for the high solid solubility of Mg in Al. Nevertheless, the electronegativity of Li and Zn gradually deviates from that of Al as the applied pressure increases, which may be one of the reasons for the limited solid solubility of Li and Zn in Al at high pressures. Overall, pressure can reduce the λ value and the electronegativity difference (from 0.306 eV at ambient pressure to 0.286 eV at 10 GPa in $Al_{55}Mg_{35}Li_5Zn_5$), thereby facilitating the formation of a single-phase solid solution.

Generally, high configurational entropy also favors the formation of a random solid solution at high temperatures. Could we rationalize the formation of the SP-FCC $Al_{55}Mg_{35}Li_5Zn_5$ CCA from an entropy perspective? The main configurational entropy term of the CCAs is considered as the configurational entropy of mixing for an ideal solution (denoted as S_C), and the S_C of $Al_{55}Mg_{35}Li_5Zn_5$ is 8.28 J mol^{-1} K^{-1}. The total configurational entropy of mixing (denoted as S_T) can be written as $S_T = S_C + S_E$, where S_E denotes the excess configurational entropy of mixing, which excludes the contribution from an ideal solution and can be related to the atomic size misfit in the atomic packing[36–39]. Based on the variation of atomic size with pressure for four components, S_E as a function of pressure can be estimated (Fig. 5d). As can be seen, the S_E value of $Al_{55}Mg_{35}Li_5Zn_5$ shows a rapid increase during compression to 20 GPa, resulting in an increase in the total configurational entropy of mixing.

Therefore, the formation mechanism for the SP-FCC of $Al_{55}Mg_{35}Li_5Zn_5$ at 10 GPa above ~ 950 K can be summarized from the following aspects. Firstly, no SP-FCC forms either by melt quenching at ambient pressure or applying pressure at room temperature. As shown in Fig. 4, both pressure and temperature play important roles in the formation of SP-FCC phase. High pressure can decrease the differences in atomic size and electronegativity between the solute elements and Al, thus enhancing the solubility of Mg, Li, and Zn in Al. In addition, pressure can also increase the total configurational entropy of the alloy, and so does elevating temperature. Increase in the configurational entropy tends to decrease the total free energy, which thermodynamically stabilizes solid solution against IMCs at high enough temperatures[40]. Moreover, long-range atomic diffusion is needed to form a single phase from the initial multiphase mixture containing IMCs. As such, the single-phase solid solution can only be formed under sufficiently high pressure and high temperature. The synthesized SP-FCC phase was fully reserved as a metastable phase to ambient conditions, which may be attributed to the typical low atomic diffusion and high energy barrier caused by the complex compositions in CCAs[41,42].

HPHT seems to be an effective way to explore lightweight Al alloys by increasing the solid solubility of other light components in Al. For demonstration of its generality, three other alloys, $Al_{60}Mg_{40}$, $Al_{50}Mg_{50}$, and $Al_{40}Mg_{40}Li_{10}Zn_{10}$ were investigated under similar HPHT

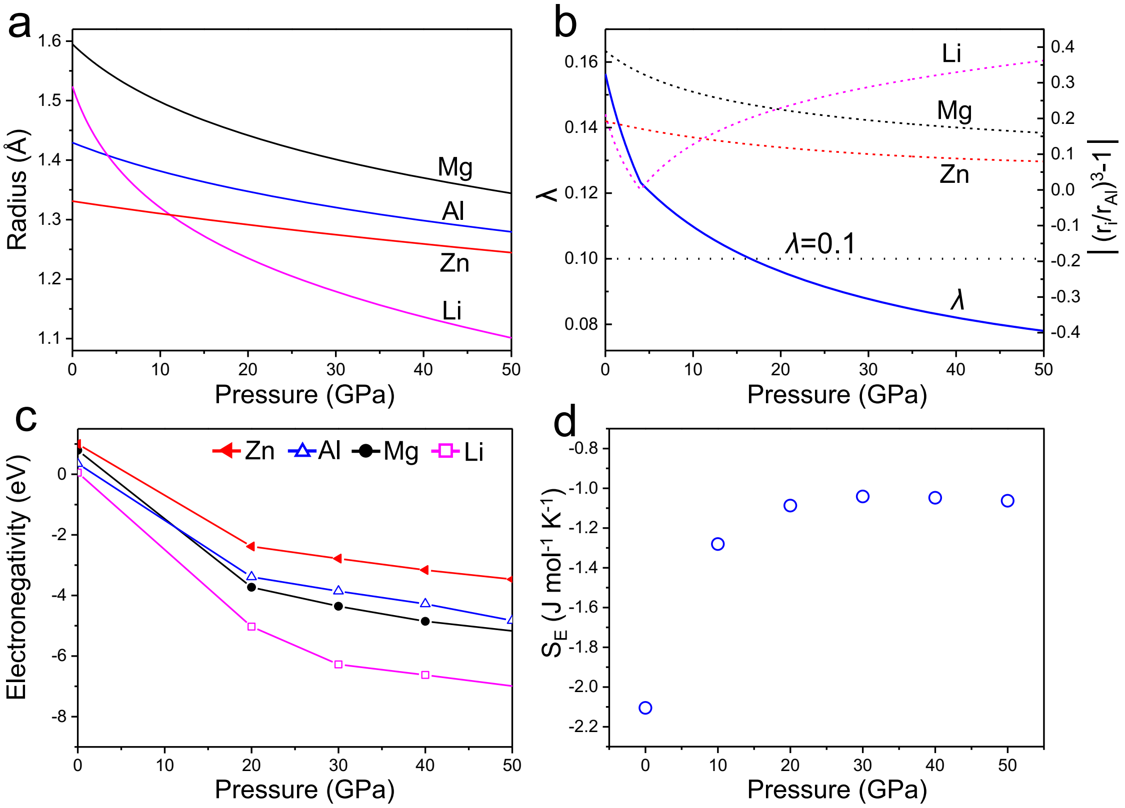

Fig. 5 | Change of radius, local atomic strain (*λ*), electronegativity, and excess configurational entropy (S_E) as a function of applied pressure. **a** Pressure-Radius relationship for four components up to 50 GPa. The radius under high pressure was determined by high-pressure volume data of four components from literature[31–35]. **b** The local atomic strain (*λ*) as a function of pressure in $Al_{55}Mg_{35}Li_5Zn_5$. The left y-axis shows the *λ* parameter as a function of pressure (blue solid curve) while the right y-axis presents the separate contribution from each solute atom (Mg, Li, and Zn) to the *λ* parameter as a function of pressure (dashed lines). The dotted horizontal line marks the position where $\lambda = 0.1$. **c** The electronegativity of four components as a function of pressure. **d** The change of excess configurational entropy (S_E) with pressure in $Al_{55}Mg_{35}Li_5Zn_5$.

conditions, and their final products were characterized using synchrotron XRD (Supplementary Fig. 2). SP-FCC solid solutions were successfully synthesized in $Al_{60}Mg_{40}$ and $Al_{50}Mg_{50}$ (with $\lambda \le 0.11$), while the formation of a SP-FCC structure is unattainable in $Al_{40}Mg_{40}Li_{10}Zn_{10}$ alloy within the pressure range of 5-40 GPa up to 2000 K (corresponding to *λ* values greater than 0.11). Based on these results, we can determine the necessary condition for the formation of a single-phase solid solution in this alloy system is that the critical value must be no less than 0.11, namely $\lambda \le 0.11$. It is important to point out that pressure can decrease the electronegativity difference within the alloy, a single phase could form with a larger λ value. The synthesis of SP-FCC CCA in this work is by no means limited to this specific $Al_{55}Mg_{35}Li_5Zn_5$ composition, and we expect that *λ* and electronegativity difference could serve as a guiding principle for single-phase synthesis in various CCAs at certain pressure and temperature conditions.

The SP-FCC solid solution $Al_{55}Mg_{35}Li_5Zn_5$ CCA shows superior mechanism properties to the as-cast alloy and many other typical lightweight CCAs. The strengthening mechanism is believed to lie in its composition and microstructure. The partial recovery of the differences in atomic sizes of the four elements at RT and ambient pressure results in substantial atomic strain fluctuations in the SP-FCC $Al_{55}Mg_{35}Li_5Zn_5$ CCA, which was verified by the geometric phase analysis results (see Supplementary Note 4 and Supplementary Fig. 10). Accordingly, the resulting nanoscale strain fields led to considerable resistance to dislocation gliding, contributing substantially to the strengthening[43].

Firstly, to account for the solid solution strengthening effect in this CCA, the framework of an existing solute strengthening theory for CCAs[44,45] was used. Two fundamental quantities, the zero-temperature yield stress, τ_{y0}, and the zero-stress energy barrier, ΔE_b, were first computed:

$$\tau_{y0} = 0.01785\alpha^{-\frac{1}{3}}\bar{\mu}\left(\frac{1+\bar{\nu}}{1-\bar{\nu}}\right)^{\frac{4}{3}}\left[\frac{\sum_n c_n \Delta V_n^2}{b^6}\right]^{\frac{2}{3}} \tag{1}$$

$$\Delta E_b = 1.5618\alpha^{\frac{1}{3}}\bar{\mu}b^3\left(\frac{1+\bar{\nu}}{1-\bar{\nu}}\right)^{\frac{2}{3}}\left[\frac{\sum_n c_n \Delta V_n^2}{b^6}\right]^{\frac{1}{3}} \tag{2}$$

where *b* is the Burgers vector (0.286 nm for Al), $\alpha = 0.125$ is the edge dislocation line tension parameter, accurate for a number of FCC metals. For elastic constants of the alloy, we used a rule-of-mixtures based on the elemental (isotropic polycrystalline) elastic constants E_n, μ_n, and ν_n (elastic modulus, shear modulus, and Poisson's ratio, respectively) for each constituent. Specifically, $\bar{E} = \sum_n c_n E_n$, $\bar{\mu} = \sum_n c_n \mu_n$, and $\bar{\nu} = \bar{E}/2\bar{\mu} - 1$. For the misfit volumes ΔV_n, we used the Vegard's law combined with the atomic volumes $V_n = a_n^3/4$ of the FCC pure elements of lattice constants a_n. The atomic volumes for BCC (body-centered cubic) pure elements are expressed as $V_n = a_n^3/2$. For HCP (hexagonal close-packed) pure elements, $V_n = \sqrt{3}a_n^3\frac{c}{a}/4$, where $\frac{c}{a}$ is axial ratio. The atomic volume of random alloys was thus computed as $\bar{V} = \sum_n c_n V_n$ and the misfit volumes as $\Delta V_n = V_n - \bar{V}$.

At temperature T and strain rate $\dot{\epsilon}$, standard thermal activation theory then leads to the predicted yield strength as:

$$\tau_y(T,\dot{\epsilon}) = \tau_{y0}\left[1 - \left(\frac{kT}{\Delta E_b}\ln\frac{\dot{\epsilon}_0}{\dot{\epsilon}}\right)\right]^{\frac{2}{3}} \quad (3)$$

where $\dot{\epsilon}_0$ is a reference strain rate estimated to be $10^4\,s^{-1}$. The uniaxial yield strength σ_y of an isotropic polycrystal was obtained by multiplying τ_y by the Taylor factor 3.06. Application of the theory at $T = 300$ K and strain rate $5{\times}10^4\,s^{-1}$ leads to a predicted strength of 446 MPa.

Secondly, a fairly uniform distribution of dislocations was introduced into the alloy during the HPHT treatment. These dislocations interact with each other and impede their movement and result in the dislocation strengthening $\Delta\sigma_D$, which can be estimated by the following equation[46]:

$$\Delta\sigma_D = M\alpha Gb\rho^{1/2} \quad (4)$$

where α is a constant equal to 0.2, G is the shear modulus (26.9 GPa for Al-based alloys) and ρ is the dislocation density, which can be estimated by the TEM result. Based on the image in Fig. 1d, the dislocation density was determined to be ~ $5.33 \times 10^{13}\,m^{-2}$, and the yield strength increment from dislocation strengthening was then calculated as ~ 34 MPa.

In addition, grain-boundary strengthening of the current CCA can be evaluated from the Hall-Petch equation expressed as:

$$\Delta\sigma_{GB} = Kd^{-1/2} \quad (5)$$

where K is a material constant equal to 0.12 $MPa/m^{1/2}$ for Al-based alloys[47], and d is the average grain diameter of ~ 100 μm, which was estimated from Fig. 1e. The strength increase due to grain-boundary strengthening was thus calculated as ~ 10 MPa, which is nearly negligible.

Lastly, based on studies in high-entropy alloys, nanoscale chemical fluctuations along dislocations may also inhibit the movement of dislocations and play an important role in strengthening the current alloys[26,48,49]. In the present case, we can assume that all clusters form along dislocation lines. Thus, the strengthening of nanoscale clusters can be approximated by dislocation dynamics simulations[50–52] as:

$$\Delta\sigma_{cl} = 0.82\left(\frac{\Omega_{cl}\ln(2D/b)}{\Omega_\infty\ln(l/b)}\right)^{3/2}\frac{Gb\ln(l/b)}{2\pi l} \quad (6)$$

where Ω_∞ is a constant (~ 4.5 GPa), l is the average planar spacing between defects: $l=1/\sqrt{DC}$ (C and D represent the number density and average size of clusters, respectively). Ω_{cl} is the shear resistance of the clusters: $\Omega_{cl} = \tau_{\max}(l_1 + l_2 + 2D)/2D$ (l_1 and l_2 represent the length of two free dislocation segments around the cluster, and $\tau_{\max}$ is the unpinning stress of dislocations, utilizing the yield strength of 825 MPa in this context). The parameters l_1, l_2, C, and D were obtained through statistical analysis of APT data (see Supplementary Fig. 11 and Table 3 for detailed analyses of the data), which are 2.1 nm, 2.1 nm, $1.02 \times 10^{24}\,m^{-3}$, and 4.8 nm respectively. Based on these data, the calculated value for Ω_{cl} is 1.44 GPa. Therefore, the contribution of nanoscale chemical fluctuations to the strength of the alloy was estimated to be ~ 42 MPa. Overall, the principal strengthening mechanisms in the synthesized SP-FCC Al-based CCA result from a combination of various factors, among which high solid solution, dislocations, and nanoscale chemical fluctuations play an important role. Supplementary Fig. 12 provides a brief summary of this.

From the standpoint of plastic deformation, planar slip dominated the deformation process with presence of massive dislocations, as exhibited in Fig. 3c. It is well known that the confinement of dislocation movement owing to the local chemical complexity of solid solution atoms[53] and a low stacking fault energy SFE essentially trigger the planarity of slip. In the synthesized SP-FCC $Al_{55}Mg_{35}Li_5Zn_5$ CCA, local chemical complexity induced by a high content of solute atoms was observed (Fig. 1f). Therefore, during the deformation process, as the first dislocation glides through the area with local chemical complexity, it needs to overcome the energy barrier associated with the nanoclusters[54]. Once the local chemical complexity is destroyed by the leading dislocations, it cannot be restored by subsequent dislocations because of its short-range nature. Hence, once a dislocation source is activated, the following dislocations tend to glide on the same plane due to the lower energy barrier, resulting in localized planar slip[54]. In addition, the addition of Mg, Li, and Zn to Al leads to a reduction in SFE compared with more dilute solutions or pure metals[55–57], which might also facilitate the slip planarity.

To further improve the plastic deformation ability of the HPHT-synthesized $Al_{55}Mg_{35}Li_5Zn_5$ CCA, introducing structural inhomogeneity at various scales, along with additional segregation and precipitations, could be an effective approach for future efforts. These structural heterogeneities can facilitate cross-slip, prompting a shift in the plastic deformation mode from planar slip to wavy slip and ultimately enhancing ductility. This work has established general design criteria for achieving single-phase solid solution CCAs at high pressure and high temperature. This introduces an approach for creating diverse and innovative lightweight CCAs with superior properties, extending the general development of CCAs into an unexplored two-dimensional pressure-temperature space.

Methods

Sample preparation

Al-Mg-Li-Zn alloy ingots with a nominal chemical composition of $Al_{55}Mg_{35}Li_5Zn_5$, $Al_{60}Mg_{40}$, $Al_{50}Mg_{50}$, and $Al_{40}Mg_{40}Li_{10}Zn_{10}$ were synthesized by induction-melting a mixture of pure metals (purity > 99.9 wt.%) under a high-purity argon atmosphere. The ingots were then cast into a cast iron mold, followed by furnace cooling to obtain rod samples. The actual composition of the SP-FCC $Al_{55}Mg_{35}Li_5Zn_5$ sample were measured by 3D-APT (see Supplementary Table 4), which matches the target well.

For the DAC study, we utilized the single-roller melting-spinning method under a high-purity argon atmosphere to prepare samples with small grains. The crystal structure of these samples was found to be consistent with that of the as-cast alloy, as depicted in Supplementary Fig. 13. The sample surfaces were polished using 5000-grit SiC paper to eliminate scratches. Subsequently, the samples were cut into pieces with a dimension of approximately 60 μm in length and 25 μm in thickness, then loaded into DACs with a culet size of 400 μm. Rhenium was used as gaskets with a 120-150 μm diameter hole drilled in the center of an indent to serve as the sample chamber. Sodium chloride was loaded as the pressure-transmitting medium and thermal insulator. Prior to use, the sodium chloride underwent a drying process at 120°C for at least 12 h to eliminate any water content. Pressure was measured by the fluorescence of a ruby ball, which was loaded into the DAC along with the sample. A double-side YLF laser-heating system was used to heat the sample at different pressures. Temperature measurements were derived by fitting the thermal radiation spectra of the heated sample to the Planck radiation function. The experimental procedure involved compressing the sample to target high pressure, followed by heating it to high temperatures. After laser heating, the pressure was released, and the sample was recovered from the DAC for further characterization at ambient conditions.

For the LVP study, master ingots prepared via induction melting were drop-casted into a copper mold with a dimension of ϕ 2 mm × 3 mm. High-pressure and high-temperature experiments were conducted using a Kawai-type multi-anvil apparatus. The sample was loaded into a boron nitride capsule, serving as an insulator. For heating, a cylindrical rhenium resistance heater surrounding the capsule was utilized. This capsule, along with the rhenium heater, was positioned within a 10 mm edge length MgO octahedron, serving as the pressure medium. The assembly was compressed with eight inner tungsten carbide cubes (second stage) with corner truncations, which were compressed synchronously with six outer (first stage) anvils. Sample temperatures were measured using a $W_{97}Re_3$-$W_{75}Re_{25}$ thermocouple, with the hot junction at the bottom of the sample capsule. The applied pressure on the sample was estimated based on the pressure generated within the multi-anvil apparatus, calibrated as a function of hydraulic oil pressure. The assembly was pressurized at ambient temperature to the target pressure, followed by heating at the target pressure to high temperature for a preset duration, and finally quenched. Subsequently, the assembly was decompressed, and the sample was retrieved for further investigation.

Characterization methods

Phase constitution and microstructure of the alloys were characterized using XRD with Cu $K\alpha$ radiation, Zeiss Supra55 SEM equipped with EDS, and TEM (Tecnai G2 F30, 300 kV). Nanoscale chemical analysis was conducted using a LEAP-5000XR APT. Specimens for TEM and APT tests were prepared using a focused ion beam (FEI versa 3D). Synchrotron XRD experiments were performed on the recovered samples at beamline 12.2.2 of the Advanced Light Source, Lawrence Berkeley National Laboratory. The X-ray wavelength used was 0.5391 Å. Data collection utilized a MAR345 image plate detector. Some of our samples were also checked at beamline 15U1 of the Shanghai Synchrotron Radiation Facility, China with X-ray wavelength of 0.6199 Å. The obtained XRD patterns were analyzed using Dioptas software.

In situ laser heating XRD measurements at different pressures

To investigate the phase transformation from IMCs to an SP-FCC structure in the $Al_{55}Mg_{35}Li_5Zn_5$ CCA, we conducted in situ high-pressure XRD and in situ HPHT laser heating XRD measurements at beamline 13-ID-D, Advanced photon source (APS), Argonne National Laboratory (ANL). For these experiments, we utilized an online laser heating system coupled with a DAC to enable double-sided laser heating of the sample at high pressures. Supplementary Fig. 14 illustrates the experimental set-up of the DAC, along with a representative image of a DAC sample. The X-ray wavelength employed was 0.3344 Å. Sodium chloride was the pressure-transmitting medium, pressure standard, and thermal insulator. Temperature determination involved fitting the blackbody radiation spectra of the heated sample on both sides to the Planck radiation function.

Mechanical tests

Room-temperature compressive tests were performed on a CMT4305 universal electronic testing machine at a strain rate of $5\times10^{-4}\,s^{-1}$. A strain gauge (YYJ-4/14-Y) was employed to measure the deformation strain of materials. Cylindrical samples with a diameter of 2 mm and a height of 3 mm were tested. Compressive tests were conducted three times for both the as-cast and SP-FCC samples. An offset (0.2%) yield strength was utilized as the yield strength (see Supplementary Fig. 15 for details).

Calculation of electronegativity under high pressures

The electronegativity values of elements under high pressure are calculated using charged He-matrix method[30], in which structure relaxations and enthalpy calculations were performed using density functional theory (DFT) within the Perdew-Burke-Ernzerhof (PBE) functional[58] in the framework of the all-electron projector augmented wave (PAW) method[59] as implemented in the VASP code[60]. We used a plane-wave kinetic energy cutoff of 1000 eV, and the Brillouin zone was sampled with a resolution of $2\pi\times0.03\,Å^{-1}$, which showed excellent convergence of the energy differences, stress tensors, and structural parameters. The calculations included scalar relativistic effects.

Calculation of the entropy

The configurational entropy of mixing (S_C) can be given by the regular solution model[61] as:

$$S_C = -R\sum_{i=1}^{m} x_i \ln(x_i) \tag{7}$$

where x_i is the mole fraction of element i, m is the number of elements, and R is the ideal gas constant. For the studied $Al_{55}Mg_{35}Li_5Zn_5$ alloy, this model gives $S_C = 8.28\,J\,mol^{-1}\,K^{-1}$.

The excess configurational entropy (S_E) can be calculated by the Carnahan and Starling theory[38,39] as:

$$\frac{S_E}{k_B} = \frac{3}{2}\left(\zeta^2-1\right)y_1 + \frac{3}{2}(\zeta-1)^2 y_2 - \left[\frac{1}{2}(\zeta-1)(\zeta-3)+\ln\zeta\right](1-y_3) \tag{8}$$

where k_B is the Boltzmann constant, and ζ is a parameter being defined as $\zeta = 1/(1-\xi)$ with a packing fraction ξ. Dimensionless parameters y_1, y_2 and y_3 are defined as below:

$$y_1 = \frac{1}{\sigma^3}\sum_{j>i=1}^{3}\left(d_i+d_j\right)\left(d_i-d_j\right)^2 c_i c_j \tag{9}$$

$$y_2 = \frac{\sigma^2}{\left(\sigma^3\right)^2}\sum_{j>i=1}^{3} d_i d_j\left(d_i-d_j\right)^2 c_i c_j \tag{10}$$

$$y_3 = \frac{\left(\sigma^2\right)^3}{\left(\sigma^3\right)^2} \tag{11}$$

$$\sigma^k = \sum_{i=1}^{3} c_i d_i^k; k = 2, 3 \tag{12}$$

Here, y_1, y_2, and y_3 have a relation: $y_1 + y_2 + y_3 = 1$. d_i is an atomic diameter of the i^{th} element, and c_i is the mole fraction of the i^{th} element.

Data availability

All data that support the key findings in this study are available within the main text and the Supplementary Information file. Additional raw data are available from the corresponding authors upon request. Source data are provided with this paper.

References

1. Zhang, Q., Zhu, Y., Gao, X., Wu, Y. & Hutchinson, C. Training high-strength aluminum alloys to withstand fatigue. *Nat. Commun.* **11**, 5198 (2020).
2. Kim, S. H., Kim, H. & Kim, N. J. Brittle intermetallic compound makes ultrastrong low-density steel with large ductility. *Nature* **518**, 77–79 (2015).
3. Jeong, I. S. & Lee, J. H. Single-phase lightweight high-entropy alloys with enhanced mechanical properties. *Mater. Des.* **227**, 111709 (2023).
4. Li, Z. et al. Ultrasonic-vibration-enhanced plasticity of an entropic alloy at room temperature. *Acta Mater.* **225**, 117569 (2022).
5. Chauhan, P., Yebaji, S., Nadakuduru, V. N. & Shanmugasundaram, T. Development of a novel light weight $Al_{35}Cr_{14}Mg_6Ti_{35}V_{10}$ high entropy alloy using mechanical alloying and spark plasma sintering. *J. Alloys Compd.* **820**, 153367 (2020).

6. Kumar, A. & Gupta, M. An insight into evolution of light weight high entropy alloys: a review. *Metals* **6**, 199 (2016).
7. Maulik, O. & Kumar, V. Synthesis of $AlFeCuCrMg_x$ (x = 0, 0.5, 1, 1.7) alloy powders by mechanical alloying. *Mater. Charact.* **110**, 116–125 (2015).
8. Yang, X., Chen, S. Y., Cotton, J. D. & Zhang, Y. Phase stability of low-density, multiprincipal component alloys containing aluminum, magnesium, and lithium. *Jom* **66**, 2009–2020 (2014).
9. Nagase, T., Terayama, A., Nagaoka, T., Fuyama, N. & Sakamoto, T. Alloy design and fabrication of ingots of Al-Mg-Li-Ca light-weight medium entropy alloys. *Mater. Trans.* **61**, 1369–1380 (2020).
10. Chaskis, S., Stachouli, E., Gavalas, E., Bouzouni, M. & Papaefthymiou, S. microstructure, phase formation and heat-treating of novel cast Al-Mg-Zn-Cu-Si lightweight complex concentrated aluminum based alloy. *Materials* **15**, 3169 (2022).
11. Sadeghi, M. & Niroumand, B. Design and characterization of a novel MgAlZnCuMn low melting point light weight high entropy alloy (LMLW-HEA). *Intermetallics* **151**, 107658 (2022).
12. Liu, C. T. & Stiegler, J. O. Ductile ordered intermetallic alloys. *Science* **226**, 636–642 (1984).
13. Feng, R. et al. Design of light-weight high-entropy alloys. *Entropy* **18**, 333 (2016).
14. Zeng, Q. S. et al. Substitutional alloy of Ce and Al. *Proc. Natl. Acad. Sci. USA.* **106**, 2515–2518 (2009).
15. Zhang, F. et al. Polymorphism in a high-entropy alloy. *Nat. Commun.* **8**, 15687 (2017).
16. Zhang, L., Wang, Y., Lv, J. & Ma, Y. Materials discovery at high pressures. *Nat. Rev. Mater.* **2**, 1–16 (2017).
17. Bykov, M. et al. High-pressure synthesis of ultraincompressible hard rhenium nitride pernitride $Re_2(N_2)(N)_2$ stable at ambient conditions. *Nat. Commun.* **10**, 2994 (2019).
18. Tian, Y. et al. Ultrahard nanotwinned cubic boron nitride. *Nature* **493**, 385–388 (2013).
19. Huang, Q. et al. Nanotwinned diamond with unprecedented hardness and stability. *Nature* **510**, 250–253 (2014).
20. Jie, J., Zou, C., Wang, H. & Wei, Z. Microstructure evolution of Al-Mg alloy during solidification under high pressure. *Mater. Lett.* **64**, 869–871 (2010).
21. Liu, X. et al. Solidification of Al-xCu alloy under high pressures. *J. Mater. Res. Technol.* **9**, 2983–2991 (2020).
22. Wu, W., Peng, Q., Guo, J. & Zhao, S. Phase transformation of Mg-Li alloys induced by super-high pressure. *Mater. Lett.* **117**, 45–48 (2014).
23. Sun, W. T. et al. Altered ageing behaviour of a nanostructured Mg-8.2Gd-3.8Y-1.0Zn-0.4Zr alloy processed by high pressure torsion. *Acta Mater.* **151**, 260–270 (2018).
24. Kirchheim, R. Reducing grain boundary, dislocation line and vacancy formation energies by solute segregation. I. Theoretical background. *Acta Mater.* **55**, 5129–5138 (2007).
25. Turlo, V. Dislocations as a tool for nanostructuring advanced materials. *Physchem* **1**, 225–231 (2021).
26. Wang, Y. et al. Enhancing properties of high-entropy alloys via manipulation of local chemical ordering. *J. Mater. Sci. Technol.* **180**, 23–31 (2024).
27. Martyushev, L. M. & Seleznev, V. D. Maximum entropy production principle in physics, chemistry and biology. *Phys. Rep.* **426**, 1–45 (2006).
28. Egami, T. & Waseda, Y. Atomic size effect on the formability of metallic glasses. *J. Non-Cryst. Solids* **64**, 113–134 (1984).
29. Sá Lisboa, R. D., Bolfarini, C., Botta, F. & Kiminami, C. S. Topological instability as a criterion for design and selection of aluminum-based glass-former alloys. *Appl. Phys. Lett.* **86**, 21 (2005).
30. Dong, X., Oganov, A. R., Cui, H., Zhou, X. F. & Wang, H. T. Electronegativity and chemical hardness of elements under pressure. *Proc. Natl. Acad. Sci. USA.* **119**, e2117416119 (2022).
31. Young, D. A., Cynn, H., Söderlind, P. & Landa, A. Zero-Kelvin compression isotherms of the elements $1 \le Z \le 92$ to 100 GPa. *J. Phys. Chem. Ref. Data* **45**, 043101 (2016).
32. Dewaele, A., Loubeyre, P. & Mezouar, M. Equations of state of six metals above 94 GPa. *Phys. Rev. B* **70**, 094112 (2004).
33. Dewaele, A., Torrent, M., Loubeyre, P. & Mezouar, M. Compression curves of transition metals in the Mbar range: Experiments and projector augmented-wave calculations. *Phys. Rev. B* **78**, 104102 (2008).
34. Guillaume, C. L. et al. Cold melting and solid structures of dense lithium. *Nat. Phys.* **7**, 211–214 (2011).
35. Stinton, G. W. et al. Equation of state and high-pressure/high-temperature phase diagram of magnesium. *Phys. Rev. B* **90**, 134105 (2014).
36. Zhang, X. et al. Pressure-induced local structural crossover in a high-entropy metallic glass. *Phys. Rev. B* **105**, 224201 (2022).
37. Luan, H. et al. High-entropy induced a glass-to-glass transition in a metallic glass. *Nat. Commun.* **13**, 2183 (2022).
38. Mansoori, G. A., Carnahan, N. F., Starling, K. E. & Leland, T. W. Equilibrium thermodynamic properties of the mixture of hard spheres. *J. Chem. Phys.* **54**, 1523–1525 (1971).
39. Guo, J., Bian, X., Li, X. & Zhang, C. Evaluation of liquid fragility for glass-forming alloys based on mixing enthalpy and mismatch entropy. *Intermetallics* **18**, 933–937 (2010).
40. Ye, Y. F., Wang, Q., Lu, J., Liu, C. T. & Yang, Y. The generalized thermodynamic rule for phase selection in multicomponent alloys. *Intermetallics* **59**, 75–80 (2015).
41. Yeh, J. W. Alloy design strategies and future trends in high-entropy alloys. *Jom* **65**, 1759–1771 (2013).
42. Tsai, K. Y., Tsai, M. H. & Yeh, J. W. Sluggish diffusion in Co-Cr-Fe-Mn-Ni high-entropy alloys. *Acta Mater.* **61**, 4887–4897 (2013).
43. Ding, Q. et al. Tuning element distribution, structure and properties by composition in high-entropy alloys. *Nature* **574**, 223–227 (2019).
44. Varvenne, C., Luque, A. & Curtin, W. A. Theory of strengthening in fcc high entropy alloys. *Acta Mater.* **118**, 164–176 (2016).
45. Varvenne, C. & Curtin, W. A. Predicting yield strengths of noble metal high entropy alloys. *Scr. Mater.* **142**, 92–95 (2018).
46. Bailey, J. E. & Hirsch, P. B. The dislocation distribution, flow stress, and stored energy in cold-worked polycrystalline silver. *Philos. Mag.* **5**, 485–497 (1960).
47. Ma, K. et al. Mechanical behavior and strengthening mechanisms in ultrafine grain precipitation-strengthened aluminum alloy. *Acta Mater.* **62**, 141–155 (2014).
48. Bu, Y. et al. Local chemical fluctuation mediated ductility in body-centered-cubic high-entropy alloys. *Mater. Today* **46**, 28–34 (2021).
49. Wu, Y. et al. Short-range ordering and its effects on mechanical properties of high-entropy alloys. *J. Mater. Sci. Technol.* **62**, 214–220 (2021).
50. Monnet, G. Multiscale modeling of precipitation hardening: application to the Fe-Cr alloys. *Acta Mater.* **95**, 302–311 (2015).
51. Pascuet, M. I. et al. Solute precipitation on a screw dislocation and its effects on dislocation mobility in bcc Fe. *J. Nucl. Mater.* **519**, 265–273 (2019).
52. Pascuet, M. I., Martínez, E., Monnet, G. & Malerba, L. Solute effects on edge dislocation pinning in complex alpha-Fe alloys. *J. Nucl. Mater.* **494**, 311–321 (2017).
53. An, X. H., Wu, S. D., Wang, Z. G. & Zhang, Z. F. Significance of stacking fault energy in bulk nanostructured materials: Insights from Cu and its binary alloys as model systems. *Prog. Mater. Sci.* **101**, 1–45 (2019).
54. Niu, R. et al. Mechanical properties and deformation behaviours of submicron-sized Cu-Al single crystals. *Acta Mater.* **223**, 117460 (2022).
55. Lee, B. H., Kim, S. H., Park, J. H., Kim, H. W. & Lee, J. C. Role of Mg in simultaneously improving the strength and ductility of Al-Mg alloys. *Mater. Sci. Eng. A* **657**, 115–122 (2016).

56. Schulthess, T. C., Turchi, P. E. A., Gonis, A. & Nieh, T. G. Systematic study of stacking fault energies of random Al-based alloys. *Acta Mater.* **46**, 2215–2221 (1998).
57. Qi, Y. & Mishra, R. K. Ab initiostudy of the effect of solute atoms on the stacking fault energy in aluminum. *Phys. Rev. B* **75**, 224105 (2007).
58. Perdew, J. P., Burke, K. & Ernzerhof, M. Generalized gradient approximation made simple. *Phys. Rev. Lett.* **77**, 3865–3868 (1996).
59. Blochl, P. E. Projector augmented-wave method. *Phys. Rev. B* **50**, 17953 (1994).
60. Kresse, G. & Furthmuller, J. Efficiency of ab-initio total energy calculations for metals and semiconductors using a plane-wave basis set. *Comput. Mat. Sci.* **6**, 15–50 (1996).
61. Miracle, D. B. & Senkov, O. N. A critical review of high entropy alloys and related concepts. *Acta Mater.* **122**, 448–511 (2017).
62. Shao, L. et al. A low-cost lightweight entropic alloy with high strength. *J. Mater. Eng. Perform.* **27**, 6648–6656 (2018).
63. Sanchez, J. M., Vicario, I., Albizuri, J., Guraya, T. & Acuña, E. M. Design, microstructure and mechanical properties of cast medium entropy aluminium alloys. *Sci. Rep.* **9**, 6792 (2019).
64. Li, R., Gao, J. C. & Fan, K. Study to microstructure and mechanical properties of Mg containing high entropy alloys. *Mater. Sci. Forum* **650**, 265–271 (2010).
65. Hammond, V. H., Atwater, M. A., Darling, K. A., Nguyen, H. Q. & Kecskes, L. J. Equal-channel angular extrusion of a low-density high-entropy alloy produced by high-energy cryogenic mechanical alloying. *Jom* **66**, 2021–2029 (2014).
66. Tun, K. S., Nahata, A., Vincent, S. & Gupta, M. Processing, microstructure and mechanical characterization of a new magnesium based multicomponent alloy. *Mater. Today: Proc.* **28**, 1044–1047 (2020).
67. Liao, Y. C. et al. Designing novel lightweight, high-strength and high-plasticity $Ti_x(AlCrNb)_{100-x}$ medium-entropy alloys. *Intermetallics* **117**, 106673 (2020).
68. Stepanov, N. D., Shaysultanov, D. G., Salishchev, G. A. & Tikhonovsky, M. A. Structure and mechanical properties of a lightweight AlNbTiV high entropy alloy. *Mater. Lett.* **142**, 153–155 (2015).
69. Yurchenko, N. Y., Stepanov, N. D., Shaysultanov, D. G., Tikhonovsky, M. A. & Salishchev, G. A. Effect of Al content on structure and mechanical properties of the $Al_xCrNbTiVZr$ (x=0; 0.25; 0.5; 1) high-entropy alloys. *Mater. Charact.* **121**, 125–134 (2016).

Acknowledgements

This research was supported by the National Natural Science Foundation of China (grant no. 52225103, 52061135207 to Y.W., grant no. 51871054 to Q.S.Z., and grant no. 51921001 to Z.P.L.), 111 Project (B07003 to Z.P.L), National Key Research and Development Program of China (2022YFB4602101 to Y.W.), the Projects of SKLAMM-USTB, the Shanghai Science and Technology Committee, China (No. 22JC1410300), and Shanghai Key Laboratory of Material Frontiers Research in Extreme Environments, China (No. 22dz2260800). The authors would like to thank Dr. Vitali Prakapenka, Dr. Stella Chariton, Dr. Jinyuan Yan, Dr. Saori I. Kawaguchi, and Dr. Lijie Tan for their kind help with our experiments. Use of the beamline 13-ID-D (GeoSoilEnviroCARS) was supported by the National Science Foundation (NSF)-Earth Sciences (EAR-1634415). APS is supported by the DOE Office of Science (DE-AC02-06CH11357). Beamline 12.2.2 at the Advanced Light Source is a DOE Office of Science User Facility under contract no. DE-AC02-05CH11231. Portions of the XRD experiments were carried out at the beamline BL 10XU, SPring-8 under Proposal No. 2018B1055 and the beamline 15U1, Shanghai Synchrotron Radiation Facility, China.

Author contributions

Z.P.L., Q.S.Z., and Y.W. initiated and designed this research project. M.L.H., F.Z., H.B.L., Y.P.Y., X.Y.D., Z.D.Z. and Q.S.Z. synthesized and characterized the samples using diamond anvil cells. M.L.H., F.Z., B.M.Y., and H.Y.G. synthesized the samples using large volume press. M.L.H., F.Z., H.B.L., Z.D.Z., L.H.X. and Q.S.Z. performed the synchrotron X-ray experiments. X.D. carried out theoretical calculations. M.L.H. and X-B.Z. performed the mechanical tests. M.L.H., X.Y.Y., Y.J.Z., Y.Z.S. and M.Y.J. carried out the TEM and 3DAP measurements. X.Y.P., S.H., G.Y.L., X.J.L., S.H.J., H.W., A.R. and X.B.Z. participated in the discussion of the strengthening mechanism. M.L.H., F.Z., H.B.L., Z.D.Z., Y.W., Q.S.Z. and Z.P.L analyzed the data. M.L.H., Q.S.Z., Y.W., and Z.P.L wrote the paper. All authors participated in the discussion and interpretation of the results.

Competing interests

The authors declare no competing interests.

Additional information

Supplementary information The online version contains supplementary material available at https://doi.org/10.1038/s41467-024-51387-6.

Correspondence and requests for materials should be addressed to Yuan Wu, Yaozu Shen, Xiaobin Zhang or Qiaoshi Zeng.

Peer review information *Nature Communications* thanks Xianghai An and the other, anonymous, reviewer(s) for their contribution to the peer review of this work. A peer review file is available.

Reprints and permissions information is available at http://www.nature.com/reprints